THE JOURNAL OF PHYSICAL CHEMISTRY B

Article

pubs.acs.org/JPCB

Specific His_6-tag Attachment to Metal-Functionalized Polymersomes Relies on Molecular Recognition

Pascal Tanner,[†] Maria Ezhevskaya,[‡] Rainer Nehring,[†] Sabine Van Doorslaer,[‡] Wolfgang Meier,[†] and Cornelia Palivan*[,†]

[†]Department of Physical Chemistry, University of Basel, Klingelbergstrasse 80, 4056 Basel, Switzerland

[‡]Spectroscopy in Biophysics and Catalysis (SIBAC), Department of Physics, University of Antwerp, Universiteitsplein 1, B-2610 Wilrijk, Belgium

Supporting Information

ABSTRACT: The development of nanocarriers for drug/protein delivery is in focus today, as they can serve to both decrease dosages and improve localization to a desired biological compartment. A powerful tool to functionalize these carriers is specific affinity tagging supported by molecular recognition, a key principle in biology. However, the geometry of the binding region in a molecular recognition process, and thus its conformation and specificity, are in many cases poorly understood. Here, we demonstrate that short, model peptides, His_6-tags, selectively recognize Cu^{II}-trisnitrilotriacetic acid moieties (Cu^{II}-trisNTA) when exposed at the surfaces of polymer vesicles designed to serve as nanocarriers or as surfaces for proteins binding. A mixture of poly(butadiene)-*b*-poly(ethylene oxide) (PB-*b*-PEO) and Cu^{II}-trisNTA-functionalized PB-*b*-PEO diblock copolymers (10:1) self-assembles in aqueous solution, generating vesicles with a hydrodynamic radius of approximately 100 nm, as established by light scattering and TEM. Fluorescently labeled His_6 tags specifically bind to metal centers exposed on vesicles' surface, with a dissociation constant of 0.6 ± 0.2 μM, as determined by fluorescence correlation spectroscopy. The significant rearrangement in the geometry of the metal center upon peptide binding was characterized by a combination of CW-EPR, pulse-EPR, and DFT computations. Understanding the binding configuration around the metal center inside NTA pocket exposed at the surface of vesicles supports further development of efficient targetable nanocarriers that can be recognized selectively by molecular recognition in a biological environment and facilitates their immobilization on solid supports and their use in two-dimensional protein arrays.

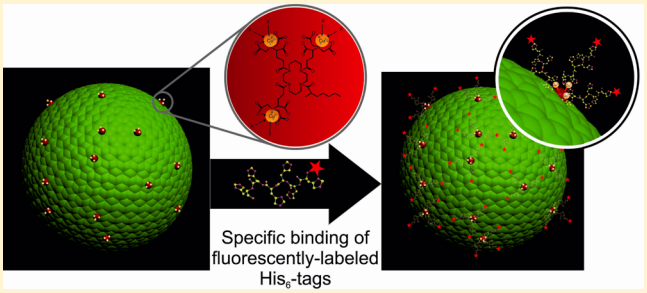

INTRODUCTION

There is a huge demand in medicine today to improve patient health by early detection of pathological conditions, or by specific and efficient therapeutic strategies. Creation of new detection methods for particular biomolecules that are to be selectively fished from a biological fluid, development of nanocarriers for target delivery of bioactive molecules, and the generation of active surfaces by immobilization of biomolecules represent challenging directions in which nanoscience is actively involved.[1] In this respect, amphiphilic copolymers that self-assemble into various supramolecular architectures, such as micelles, vesicles, tubes, and films, represent good candidates to support medical applications. For example, the polymer membrane of vesicles can be chemically selected to allow insertion/attachment of proteins, while their cavities serve to encapsulate active compounds ranging from small molecular weight drugs to proteins or DNA.[2,3] In addition, polymer vesicles with dimensions in the nanometer region, called polymersomes, are significantly more stable to lysis by classical surfactants than liposomes, while preserving low immunogenicity.[4,5] Polymersomes can be tuned to improve mechanical stability and stimuli responsiveness, and to produce specific sizes for particular routes of administration.[3,6] A powerful natural principle that governs the functionalization of polymersome surfaces for attachment to biomolecules is molecular recognition, which favors targeting approaches in therapeutics or surface immobilization.

Molecular recognition is essential in nature because it is fundamental to specific biological interactions and supports rapid, specific responses in various processes. A large variety of molecular recognition patterns exist in nature, such as antigen−antibody,[7,8] receptor−ligand systems (the nicotinic acetylcholine receptor),[9] and DNA−protein assemblies (DNA and the zinc-finger motif assembly).[10] In technology, this principle is utilized either by natural key−lock systems, or by simplified systems containing affinity tags. It supports a variety of applications, such as the purification[11,12] and immobilization[13−16] of biomolecules, labeling of proteins,[17,18] targeting approaches,[19] 2D crystallization,[13,16] and biosensing.[20,21] The surfaces of polymersomes functionalized with specific molecular

Received: June 6, 2012
Revised: July 31, 2012
Published: August 3, 2012

moieties, such as biotin, antibody, or metal complexes,[15,16] have served for their uptake in cell lines, immobilization on solid support, or protein binding.[1] In order to design polymersomes with improved functionality, it is important to understand in more detail in what respect geometry and conformation affect the recognition process by investigation of simplified systems. In particular, in assemblies that involve metals as coordination points, ligands providing open coordination sites are necessary to allow a biomolecule to interact with the metal ion by replacing the solvent molecules and rearranging the geometry.[22] In this respect, ligands such as iminodiacetato (IDA), bis(2-pyridylmethyl)amine (BPA), diethylenetriamine (DIEN), nitrilotriacetic acid (NTA), tris(2-pyridylmethyl)amine (TPA), and tri(2-aminoethyl)amine (TREN) have been extensively used to design synthetic receptors that bind peptides or proteins.[23,24]

The binding of His-tagged molecules to NTA or trisNTA (trisnitrilotriacetic acid) has been explored in terms of parameter-dependent binding affinities, such as the length of oligohistidines, multivalency of the NTA moieties, and accessibility of NTA moieties on a surface, with the aim of creating highly efficient receptor systems.[13,15,16,25−27] For example, the oligohistidine sequence consisting of six histidines, a His_6-tag, was found to efficiently interact with Ni^{II}−NTA complexes with a binding affinity in the subnanomolar range,[18,28,29] while an increased number of histidines on each tag (for example, 10 histidines instead of 6 histidines) leads to a decreased affinity for binding the metal.[22]

The affinity of different transition-metal ions, including Cu^{2+}, Fe^{3+}, Ni^{2+}, and K^+ ions, was predicted by molecular dynamic simulations, which indicated that His_6-tag exhibits the strongest binding affinity for Ni^{2+} and Cu^{2+} ions.[30] However, the detailed molecular structure of the coordination sphere around metal has not been addressed. Only one report relates to the structural determination of Cu^{II}−NTA complexes involving a bis(imidazole) ligand, whereby the pyramidal configuration obtained by X-ray diffraction has not been confirmed in solution, which is the relevant biological condition.[31] Moreover, the studies relating on small molecular weight copper−NTA-based complexes have conditions that are different to the situation of metal−NTA moieties exposed on the surface of vesicles or on a solid support.

Here, we are interested in characterizing in detail the conformational changes in the coordination sphere of a Cu^{II}−trisNTA moiety exposed at the surface of nanometer-scale polymeric vesicles undergoing the binding of His_6-tags. The system represents a simplified model of the binding of His_6-tagged proteins to metal sites at a surface, which is essential both for understanding docking in biological systems and in technical and medical applications. While the coordination sphere of Ni^{2+} ions, which are conventionally used in various NTA-based systems, is octahedral, there are various possible geometries for Cu^{II}, due to its well-known stereochemistry.[32] This flexibility of the first coordination sphere caused us to select Cu^{II} as the metal-coordination site for the His_6-tag, because the use of Cu^{II} allows us to gain more insight into the geometric rearrangement upon addition of a tag moiety. In previous studies, we and others already reported on the high affinity of different His-tagged proteins toward metal−NTA-functionalized liposomes and poly(butadiene)-*b*-poly(ethylene oxide) (PB-*b*-PEO) diblock copolymer vesicles, which are ideally suited to serve as two-dimensional protein arrays.[13,15,16] We found that the dissociation constant of the His-tagged protein had similar values when the Ni^{II}−NTA moiety was attached at the surface of liposomes or of polymeric vesicles.[15] This indicates that the His-tagged protein binding process is mainly governed by the local metal environment and much less by the surface on which the metal−NTA moieties are anchored.

In this study, we present a detailed structural view of His_6-tag binding to copper ions coordinated with the NTA pocket at the outer surface of PB-*b*-PEO vesicles (Figure 1A). The vesicles

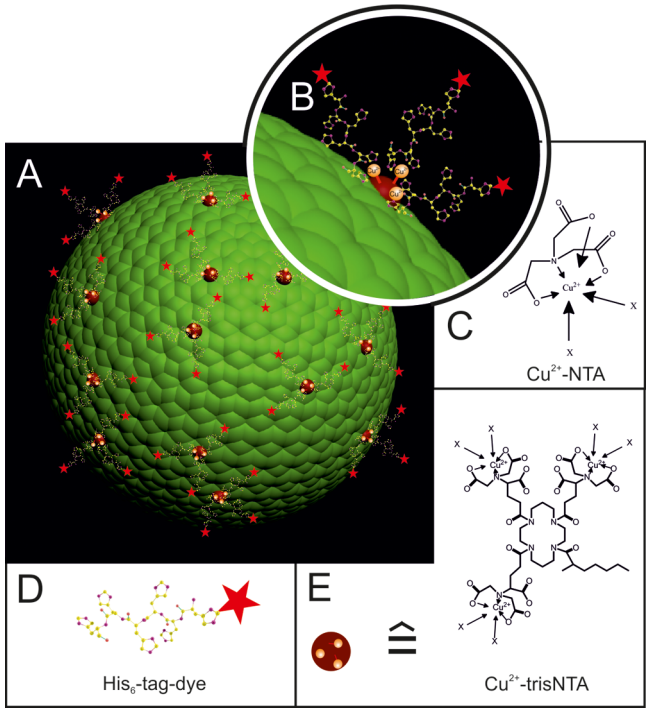

Figure 1. (A) Schematic representation of Cu^{II}-functionalized PB-*b*-PEO vesicles. The metal centers are located on the outer vesicle surface that is to be recognized by fluorescently labeled His_6-tags. (B) Detailed view of (A). (C) Schematic formula of Cu^{II}−NTA complex and (D) fluorescently labeled (sulforhodamine B) His_6-tags. (E) Cu^{II}−trisNTA. X represents solvent molecules or external binding atoms of other molecules. Red star represents sulforhodamine B.

were formed by the self-assembly of PB-*b*-PEO copolymer functionalized with trisNTA (Figure 1E). We used trisNTA because it has a binding affinity higher than NTA (Figure 1C), which will increase the probability of histidine binding. The formation of vesicles was characterized by dynamic and static light scattering and visualized by TEM and confocal laser scanning microscopy. Fluorescently labeled His_6-tags (Figure 1D) provide a simple detection method to analyze binding affinity upon molecular recognition. Fluorescence correlation spectroscopy was combined with brightness measurements to study the binding affinity of His_6-tags to Cu^{II} centers on the outer vesicle surface and to estimate the number of peptides per vesicle.

In addition, we used continuous-wave (CW) and pulsed electron paramagnetic resonance (EPR), permitting determination of the electronic and geometric structure of the coordination sphere around copper in the NTA pocket. The experimental observations are corroborated by DFT (density functional theory) computations. The observed geometric structural changes induced by His_6-tag binding both allow a zoom into the metal-coordination sphere of functionalized polymersomes with efficient binding affinity and provide details

dx.doi.org/10.1021/jp305544v | *J. Phys. Chem. B* 2012, 116, 10113−10124

for a more general modeling of His-tagged protein assemblies.[13,15,16]

MATERIAL AND METHODS

Materials. 2-(6-Chloro-1*H*-benzotriazole-1-yl)-1,1,3,3-tetramethylaminium hexafluorophosphate (HCTU) and rink amide AM resin (0.61 mmol/g) were purchased from IRIS Biotech GmbH, Marktredwitz, Germany. The amino acids (*N*-α-*t*-Boc-L-histidine) were obtained from Novabiochem, Läufelfingen, Switzerland. Sulforhodamie B acid chloride (λ_{ex} 560 nm, λ_{em} 580 nm) and copper(II)triflate was purchased from Sigma-Aldrich, Buchs, Switzerland. Dichloromethane was provided by Brenntag Schweizerhall AG, Basel, Switzerland, dimethylformamide (DMF) by J. T. Baker, and acetonitrile (ACN) by Fischer Scientific. DMF was treated with aluminum oxide to reduce the concentration of free amines prior to application in peptide synthesis.

Polymers. Synthesis and characterization of the diblock copolymer PB_{39}-*b*-PEO_{36} was described previously.[15] A mixture of PB_{39}−PEO_{36}−SA−OH containing 10% PB_{39}−PEO_{36}−SA−trisNTA.d-Cu^{2+} was used for all experiments. The diblock copolymer is functionalized with trisNTA (Figure 1E), a variant of NTA (Figure 1C) and complexed with Cu^{2+} ions. The nonfunctionalized diblock copolymer was characterized at a molecular mass of 3530 g/mol, which increased to 3690 g/mol upon functionalization with trisNTA. Both block copolymers have a low polydispersity index.[15]

Peptide Synthesis and Fluorescent Labeling. The peptides were synthesized on a Syro I Peptide Synthesizer (MulitSynTech GmbH, Witten, Germany) using solid-phase synthesis with an Fmoc strategy. HCTU was the coupling reagent, with *N*-ethyldiisopropylamine (DIPEA) dissolved in *N*-methyl-2-pyrrolidone (NMP) and used as the base to couple α-*N*-Fmoc-protected amino acids to the rink amide resin. For elongation, Fmoc−His−OH (0.5 mol/L, 4 equiv), HCTU (0.5 mol/L, 4 equiv) dissolved in DMF, and DIPEA (12 equiv) were added to the resin. The mixture was agitated for 1 h and washed with DMF (3 × 3 mL). Fmoc deprotection was performed with 20% piperidine in DMF followed by 3 min agitation, draining, and repetition of deprotection for 10 min. Resin was subsequently washed with DMF (5 × 3 mL). Acetylation of unreacted amine groups was performed following each coupling with a solution of acetic anhydride/DIPEA (3 mol/L, 5 equiv) in DMF. After synthesis, the peptide resin was alternately washed with DMF (3 × 6 mL), isopropanol (3 × 6 mL), and dichloromethane (3 × 6 mL), and then dried under vacuum.

The coupling of the dye to the N-terminus was performed on peptide still bound to the solid phase. A DMF solution of carboxylic acid succinimidyl ester activated dye (sulforhodamine B) was added to the peptide. Uncoupled dye was washed away alternating with DMF (3 × 6 mL), isopropanol (3 × 6 mL), and dichloromethane (3 × 6 mL).

Cleavage of the peptide from the resin and removal of its protective groups was performed with a mixture of 95% trifluoroacetic acid (TFA), 2.5% triisopropylsilane, and 2.5% H_2O. The resin was additionally washed two times with this mixture (2 mL), and the peptide was precipitated in 40 mL of cold diisopropyl ether (IPE). The precipitated peptide was washed three times with cold IPE by centrifugation and decantation before being dried under vacuum.

Peptide Purification and Characterization. Purification and analysis of the peptides were performed by HPLC (Shimadzu Prominence 20A, Japan) on reverse phase (RP) columns (Merck Chromolith, RP-18e, 100 mm × 10 mm and 100 mm × 4.6 mm). The separation of the unlabeled peptide from labeled peptide yielded sample purities higher than 95%. This was detected by absorption at 280 and 560 nm. Linear gradients of solvent A (ACN) and solvent B (0.1% TFA, or 2% acetic acid in bidistilled water) were used.

The eluted sample was collected in fixed volume fractions, which were subsequently analyzed for purity and molecular weight using HPLC and matrix-assisted laser desorption/ionization time-of-flight mass spectroscopy (MALDI-TOF-MS). MALDI-TOF-MS was performed for mass confirmation with a Voyager-DETM System (Applied Biosystems, USA) in positive reflector mode, an accelerating voltage of 25 kV, grid voltage of 75%, and 100−300 ns extraction delay time. Matrix (α-cyano-4-hydroxycinnamic acid) sample mixtures were prepared using a solution of ACN/0.1% TFA in bidistilled water on a 100-well gold plate. Fractions with matching mass and exceeding 95% purity were pooled with ammonia before neutralization and then lyophilized. Products were stored under argon at −18 °C.

PB-*b*-PEO Vesicle Preparation and His_6-Tag Binding. PB-*b*-PEO vesicles were prepared (800 μM) according to the film rehydration method and contained 10% Cu^{II}-trisNTA functionalized PB-*b*-PEO copolymer.[15] Sulforhodamine B acid chloride labeled His_6-tags (s-His_6-tags) were added to the vesicle solution at different concentrations depending on the used measurement technique (see below).

Dynamic and Static Light Scattering (DLS and SLS). Light-scattering experiments were performed on an ALV (Langen, Germany) goniometer, equipped with an ALV He−Ne laser (JDS Uniphase, wavelength λ = 632.8 nm). Vesicle dispersions were prepared by serial dilution to polymer concentrations ranging from 0.7 to 0.1 g/L. Light scattering was measured in 10 mm cylindrical quartz cells at angles of 30−150° at 293 K ± 0.5 K. The photon intensity autocorrelation function $g^2(t)$ was determined with an ALV-5000E correlator (scattering angles between 30° and 150°). DLS data were analyzed via nonlinear decay-time analysis supported by regularized inverse Laplace transform of $g^2(t)$ (CONTIN algorithm). The angle-dependent apparent diffusion coefficient was extrapolated to zero momentum transfer (q^2) using ALV Correlator software static and dynamic FIT and PLOT 4.31.

Transmission Electron Microscopy (TEM). TEM images were taken using a transmission electron microscope (Philips Morgagni 268D) operated at 80 keV. The vesicle samples diluted to a final polymer concentration of 8 μM were negatively stained with 2% uranyl acetate solution for 10 s and deposited on carbon-coated copper grids in order to perform the measurement.

Confocal Laser Scanning Microscope (CLSM). PB-*b*-PEO vesicles were prepared (800 μM) as mentioned above and were incubated with fluorescently labeled His_6-tags (s-His_6-tags) (1 μM) for 5 min at room temperature. The solution was dialyzed for 24 h with a Spectrapore dialysis tube (mean width cutoff size 300 kDa, Spectrum Laboratories Inc.) to separate nonbound s-His_6-tags from vesicles. This solution was investigated at room temperature in special chambered quartz glass holders with a confocal laser scanning microscope (Zeiss LSM 510-META/Confcor2), in LSM mode, using a HeNe laser (543 nm) and a 63× water-immersion objective (Zeiss C/Apochromat 63X, NA 1.2). HeNe laser excitation power was PL = 15 mW, and excitation transmission at 543 nm was 20%.

dx.doi.org/10.1021/jp305544v | J. Phys. Chem. B 2012, 116, 10113−10124

Fluorescence Correlation Spectroscopy (FCS). For FCS measurements, PB-*b*-PEO vesicle solutions with different Cu^{II} concentrations (ranging from 2 to 8 μM) were prepared as mentioned above. In addition, the solutions were extruded with an Avanti mini-extruder (Avanti Polar Lipids, AL) through a 400 nm diameter pore-size polycarbonate (PC) membrane (one time), and through a 200 nm pore-size PC membrane (11 times) in order to minimize nanovesicle size distribution. Afterward, the vesicle solutions containing different amounts of copper were incubated with 50 nM s-His_6-tags and were immediately measured without dialyzing. FCS measurements were performed at room temperature in special chambered quartz glass holders (Lab-Tek; 8-well, NUNC A/S), on the Zeiss LSM 510-META/Confcor2 laser-scanning microscope equipped with a HeNe laser (543 nm) and a 40× water-immersion objective (Zeiss C/Apochromat 40X, NA 1.2), with pinhole adjusted to 78 μm. Spectra were recorded over 30 s, and each measurement was repeated 10 times. The excitation power of the HeNe laser was PL =15 mW, and the excitation transmission at 543 nm was 10%. The structural parameter and diffusion times of the free dye (sulforhodamine B acid chloride) and of the dye-labeled His_6-tags were independently determined and fixed in the fitting procedure. These parameters were used to fit the autocorrelation curve of s-histidine-bound PB-*b*-PEO vesicles. The fluorescence signal was measured in real time and the autocorrelation function was calculated by a software correlator (LSM 510 META-ConfoCor 2 System). The results were presented as a mean value of three independent measurements.

X-Band CW-EPR. Samples for X-band CW-EPR measurements were prepared similar to FCS with the exception that an 800 μM vesicle solution was incubated with 2.0 mM s-His_6-tags. X-band CW-EPR measurements (microwave (MW) frequency of about 9.44 GHz) were performed on a Bruker ESP 300E instrument, equipped with a liquid helium cryostat (Oxford Inc.). A MW power of 10 mW, a modulation frequency of 100 kHz and a modulation amplitude of 0.5 mT were applied. All spectra were taken at 100 and 10 K. The EasySpin program was utilized to simulate the CW-EPR spectra.[33]

X-band pulsed EPR experiments were performed on a Bruker Elexsys spectrometer (9.76 GHz), equipped with a helium-gas flow cryostat (Oxford Inc.). The measurements were done at 4 K, with a repetition rate of 1 kHz.

ENDOR Experiments. The ENDOR experiments[34] were performed using the MW pulse sequence $\pi-T-\pi/2-\tau-\pi-\tau-$echo, whereby a π radio frequency (rf) pulse is applied during time T. The following parameters were used: t_π = 48 (96) ns, $t_{\pi/2}$ = 24 (48) ns, T = 15 μs, t_{rf} = 13 μs, and τ = 200 ns. The Mims ENDOR experiments were performed with the MW pulse sequence $\tau-\pi/2-\tau-\pi/2-T-\pi/2-\tau-$echo.[35] The parameters used were $t_{\pi/2}$ = 16 ns, T = 15 μs, and t_{rf} = 13 μs. The spectra were recorded at τ = 104 ns.

HYSCORE. The standard HYSCORE experiments[36] were performed using the $\pi/2-\tau-\pi/2-t_1-\pi-t_2-\pi/2-\tau-$echo sequence of pulses with $t_{\pi/2}$ = 16 ns and t_π = 16 ns. The time intervals t_1 and t_2 were varied in steps of 16 ns. In order to eliminate unwanted echoes, a four-step phase cycle was applied. The time-domain HYSCORE spectra were baseline corrected with a third-order polynomial, apodized with a Hamming window, and zero filled. The absolute-value spectra, obtained after two-dimensional Fourier transformation, were added to different τ values (104, 120, 176 ns) to reduce the blind-spot effects. The HYSCORE spectra were simulated using a program developed at ETH Zurich.[37]

DFT Computations. Spin-restricted DFT computations were performed with the ORCA package[38−41] on different models for aqueous Cu^{II}−NTA and Cu^{II}−NTA−His-tag binding (see Results and Discussion). Geometry optimizations were performed with the BP86 functional,[42−44] with an Ahlrich split-valence plus polarization (SVP) basis set for all other atoms[45,46] except copper, for which a more polarized triple-ζ valence basis set (TZVPP) is used.[45,46] The geometry optimizations were tested for different starting geometries and the most stable geometry overall was chosen for further computation of the EPR parameters. For the latter, the B3LYP functional[47] was taken, combined with the EPR-II basis set[48] for nitrogen and hydrogen, the ORCA basis set "Core Properties" (CP(PPP))[49] and SVP[45,46] for all other atoms. A dielectric surrounding with the dielectric constant of water was simulated assuming the COSMO model[50] in all computations.

RESULTS AND DISCUSSION

Formation of Cu^{II}-trisNTA PB-*b*-PEO Vesicles. The functionalization of the polymersome surface with specific moieties represents a necessary step further in supporting efficient applications, such as targeting approaches, or immobilization on solid support to generate active surfaces. One possible way for functionalization of polymer vesicles is to use the molecular recognition principle. The perfect structural matching between the molecules exposed at the surface of vesicles and the biomolecules serves to create complex polymer−biomolecule assemblies.

We previously reported that Ni^{II}-NTA-functionalized PB-*b*-PEO vesicles successfully served to bind His-tagged proteins such as His_6-enhanced green fluorescent protein (His_6-EGFP), His_6-red fluorescent protein (His_6-RFP), or His_{10}-maltose binding protein conjugated to fluorescein (His_{10}-MBP-FITC).[15,16] The molecular recognition interaction between the metal center exposed at the surface of vesicles and His-tagged proteins takes place by a rearrangement of the metal coordination sphere, when nitrogen atoms from histidines replace the weakly bound solvent molecules. Here, we chose replacing His-tagged proteins with low molecular weight molecules that mimic the structural requirements for recognition as a simple model underlying principles of complex molecular recognition assemblies.[15,16] This His_6-tag peptide model has the advantages to increase the accessibility to the NTA pocket and to support a more flexible geometry around the copper ion, which will allow us to gain more insight into the molecular recognition pattern.

Vesicles made of PB_{39}−PEO_{36}−SA−OH-containing 10% PB_{39}−PEO_{36}−SA−trisNTA.d-Cu^{2+} were formed by the film rehydration method and extruded through a 200 nm diameter pore membrane to reduce inherent vesicle polydispersity that ranged from giant vesicles (micrometer range) to nanovesicles.[15] We chose copper instead of nickel to exploit the well-known variety in copper stereochemistry and the possibility of linking fine structural changes in the metal-coordination sphere to experimental parameters obtained from EPR. The selection of copper will allow a detailed structural characterization of the NTA pocket upon binding, while preserving the high binding affinity similar to that of Ni^{2+} ions.[30]

The vesicle solutions were characterized by dynamic and static light scattering[51] and a hydrodynamic radius of R_h = 107

±12 nm was obtained (data plot is shown in the Supporting Information). This is comparable to the value found for vesicles generated from Ni^{II}-functionalized trisNTA-PB-*b*-PEO vesicles.[16] The ratio between the radius of gyration (R_G) resulting from static light scattering experiments and R_h resulting from dynamic light scattering (R_G/R_h) is 0.96, which indicates hollow-sphere morphology. As expected, the use of similar amounts of copper instead of nickel ions inside the NTA moieties exposed at the surface of polymer membranes did not affect the vesicle formation in terms of size or morphology. The unchanged morphology indicates that the metal ions are located inside the trisNTA moiety and do not destabilize the polymer membrane. Further analysis of static light scattering data (Guinier plot is shown in the Supporting Information) permitted the calculation of the weight average molecular weight of a vesicle (M_w) as $8 \times 10^7 \pm 3 \times 10^6$ g/mol and a second virial coefficient A_2 close to zero, showing that there are no long-range interactions between the vesicles in the investigated concentration range. Similar to Ni^{II}-functionalized PB-*b*-PEO vesicles, Cu^{II}-functionalized vesicles preserved their size and shape over several months at room temperature. Dividing the weight average molecular weight of a vesicle by the weight average molecular weight of the diblock copolymer, an aggregation number of around 20 000 was found, further supporting the formation of nanometer-sized vesicles. From a theoretical point of view, the number of functional metal ions can be estimated from the aggregation number. We mention that only 50% of functional groups (metal centers) are exposed at the external surface of vesicles, the rest being inside the cavity. Taking into account a 10% copper-trisNTA functionalization, a 50% probability of orienting the functional group in the same direction with respect to the membrane and a 10% yield of rehydrated diblock copolymer due to inconsistency of solubility after film rehydration, approximately 300 metal ions per vesicle can be estimated. This represents 20 metal ions per 100 nm^2 of vesicle surface: the vesicle surface is relatively dense packed with metal ions, which can be efficiently recognized by His-tagged peptides. We noticed that in the case of His_6 proteins a decrease of the number of metal ions/nm^2 of vesicles surface to favor the accessibility can be easily achieved by decreasing the amount of functionalized copolymer used for vesicles generation.

His_6-tag Binding to Cu^{II}-trisNTA PB-*b*-PEO Vesicles. It is of special interest to determine whether the copper-functionalized vesicles change their structure or tend to aggregate upon binding of His_6-tags. TEM was carried out in order to visualize the 10% copper-functionalized nanovesicles, both before and after addition of His_6-tags (Figure 2, A and B). The size of the vesicles evaluated from TEM images agrees with values obtained from light scattering. No change in morphology was observed when His_6-tags were added, proving the stability of the nanometer-sized vesicles after the recognition process. The different contrast of TEM micrographs is due to a different capillary effect generated by Cu-trisNTA-functionalized vesicles compared to that generated by His_6-tag bound Cu-trisNTA vesicles (uranyl acetate staining). In addition, the His_6-tags bound to the metal center on the outer vesicle surface were observed not to form aggregates, which could extensively influence cell uptake.

To study the His-tag binding in more detail, we visualized specially generated giant vesicles after addition of fluorescently labeled His_6-tags (s-His_6-tags) by confocal laser scanning microscopy. Most of the peptides were found to immediately bind to the vesicles. The low amount of s-His_6-tags still free in solution was removed by dialysis to reduce the background fluorescence intensity. The images of the intensive fluorescent corona correspond to fluorescent s-His_6-tags that are specifically bound to the outer vesicle surface (Figure 3A). As the polymer membrane is highly impermeable to small molecules, fluorescent s-His_6-tags did not penetrate inside vesicles, and the fluorescent corona indicates the formation of His_6-tags externally decorated vesicles. By measuring giant vesicles in different planes, we reconstituted a 3-dimensional image, showing a hollow vesicular structure (Figure 3B). These giant vesicles, as well as the nanovesicles, are highly promising in terms of molecules loading and target orientation that utilizes the molecular recognition mechanism.

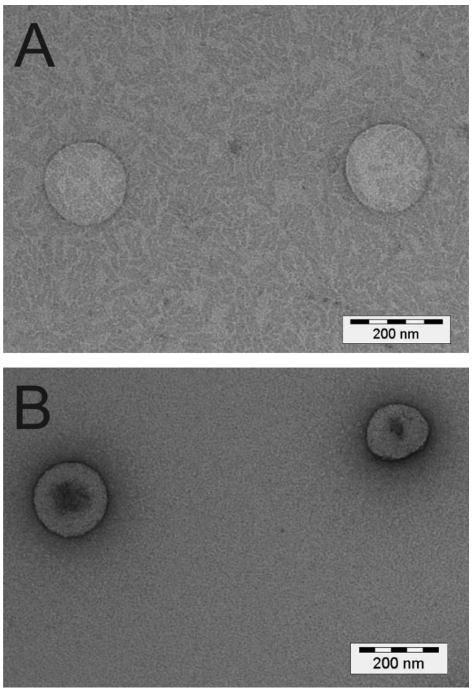

Figure 2. TEM micrograph of 10% copper-functionalized polymersomes: (A) Cu^{II}-trisNTA-functionalized PB-*b*-PEO vesicles; (B) His_6-tag bound to Cu^{II}-trisNTA-functionalized PB-*b*-PEO vesicles.

Fluorescence correlation spectroscopy has emerged as a reliable tool to investigate interactions among fluorescent molecules with very high accuracy.[52] FCS is based on the detection of random movement of fluorescent entity (molecule, particle) in a confocal volume and correlates with the information obtained by an autocorrelation function in order to determine a diffusion coefficient for the entity. Due to the fact that the diffusion time of small molecules (for example fluorescently labeled His_6-tags) is completely different from that of big entities, for example, nanovesicles, a change in the diffusion time of the fluorescently labeled His_6-tags can be directly related to their binding to the surface of nanovesicles. When Cu^{II}-functionalized vesicles were incubated with s-His_6-tags, two different populations were observed. The first population, with a diffusion time of 56 μs, represents free peptides still present in solution. The second population, with a diffusion time of 7.5 ms, represents s-His_6-tags bound to vesicles. From the point of view of population distribution, more than 95% of the s-His_6-tags were bound to vesicles (50 nM initial concentration of His_6-tag, and 8 μM Cu-trisNTA

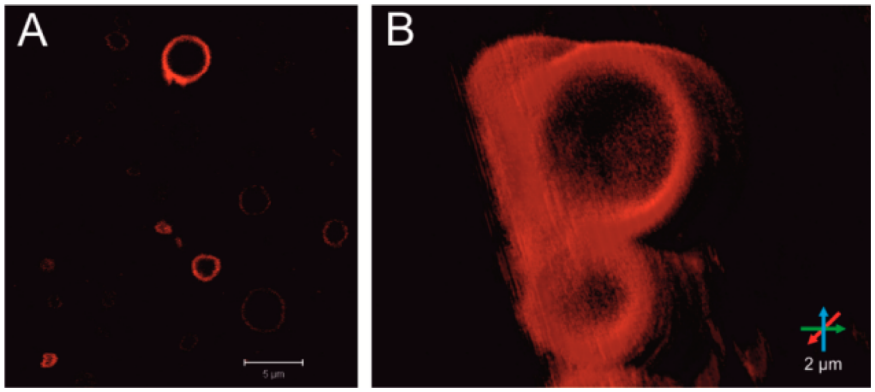

Figure 3. Confocal fluorescence microscopy image of fluorescently labeled His_6-tags bound to the outer surface of PB_{39}–PEO_{36}–SA–/10% PB_{39}–PEO_{36}–SA-trisNTA.d-Cu^{2+} (800 μM) vesicles incubated with s-His_6-tags in bidistilled water: (A) two-dimensional cut, focused on the midplane of the selected vesicles; (B) three-dimensional image produced by merging two-dimensional layers measured at different heights.

functionalized vesicles). Similar binding behavior has been observed for binding His_6-RFP to Ni^{II}-functionalized PB-*b*-PEO vesicles. This supports the use of His_6-tags as a model to test the binding properties of His-tagged proteins. Due to the smaller dimension of the model peptides, they should interfere less with the vesicle outer surface and we expect a faster binding process and stronger binding. The observation that the majority of the peptides is bound to vesicles agrees with the intense fluorescent corona of the vesicles observed in confocal microscopy (Figure 3A, B). Calculation of the hydrodynamic radius R_h via the Stoke–Einstein equation indicates a vesicle radius of 90 nm. This is comparable to the values obtained both by light-scattering characterization and by TEM, and it has the same order of magnitude as previously reported for different functionalized copolymer vesicles.[16]

In order to calculate the dissociation constant for s-His_6-tags bound to Cu^{2+}-functionalized vesicles, we titrated the s-His_6-tags (50 nM) with increasing amounts of polymer vesicles, the content of Cu^{2+} varying from 2 to 8 μM (Figure 4) (see details in Supporting Information) and fitted the curve using a Langmuir isotherm.[15,53] The dissociation constant of s-His_6-tags was calculated as 0.6 ± 0.2 μM. This is lower than the K_D calculated for His_6-RFP,[16] His_6-EGFP,[15] and His_{10}-MBP-FITC[15] when bound to polymer vesicles (Table 1).

Note that nickel-functionalized instead of copper-functionalized vesicles were used for protein binding in the studies that we compare in Table 1. According to a molecular dynamics simulation, Ni^{II} and Cu^{II} exhibit a similar affinity toward a His_6-tag.[30] However, practice has shown that Cu^{II} results in a more pronounced interaction, exemplified by higher forces needed for dissociation.[54] For example, a stronger interaction was established with histidine residues on a monolayer of lipid-IDA-Cu^{2+} as compared with lipid-IDA-Ni^{2+}.[55] Here, we found out the copper-functionalized polymer vesicles have a greater binding affinity for His_6-tags than the PB_{39}-PEO_{36}-trisNTA.d-Ni^{2+} vesicles have for His_6-RFP. In this case, the flexible PEO brushes at the surface of polymer vesicles do not interfere with the binding of peptide molecules. The smaller dissociation constant value K_D provides better conditions for protein binding and detection—thus, a selective copper-sensing system was designed using stable block copolymer vesicles. In the case of nonfunctionalized vesicles, the fraction of bound His_6-tag was less than 3% (for an initial concentration of 50 nM). This represents the unspecific His_6-tag binding to vesicles without Cu^{II}-trisNTA groups on their outer surfaces, in agreement with

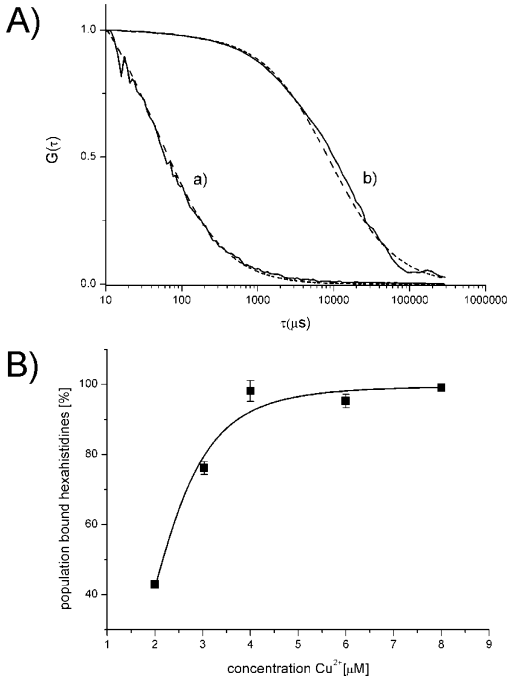

Figure 4. (A) FCS autocorrelation curves and the simulation of (a) sulforhodamine B acid chloride labeled His_6-tags and (b) sulforhodamine B acid chloride labeled His_6-tags bound to vesicles. (B) Fraction of bound s-His_6-tags as a function of the Cu^{II} content of PB_{39}–PEO_{36}–SA–OH/10%PB_{39}–PEO_{36}–SA-trisNTA-Cu^{2+} vesicles generated in bidistilled water (initial concentration of His_6-tag 50 nM, and initial concentration of Cu-trisNTA functionalized vesicles 8 μM).

the protein-repellent character of the PEO brushes at the vesicle surface.[16] In addition, vesicles generated with the nonfunctionalized copolymer after addition of $Cu(OTf)_2$ did not bound s-His_6-tags, similarly to the case of His-tag proteins.

The number of peptides/vesicle was calculated from brightness measurements by dividing the value of the molecular brightness of peptide-bound vesicles, expressed as counts per molecule (CPM), by the CPM of freely diffusing His_6-tags, taking the fluorescence quantum yield into account. On average, a value of 210 ± 36 molecules/vesicle was obtained. This is an order of magnitude higher than previously reported for His_6-RFP binding to vesicles. Considering that the size of the peptide is an order of magnitude smaller than a fluorescent protein, the available metal–trisNTA moieties on the vesicle

dx.doi.org/10.1021/jp305544v | J. Phys. Chem. B 2012, 116, 10113–10124

Table 1. Comparison of Different K_D Values in Polymer Vesicles and Liposomes Using Different His-Tagged Ligands

vesicle system	ligand	K_D (μM) (based on FCS)	ref
PB_{60}-*b*-PEO_{34}–SA/PB_{60}-*b*-PEO_{34}–SA–NTA.d-Ni^{2+}	His_6-EGFP	12.0 ± 0.8	15
PB_{39}-*b*-PEO_{36}–SA/PB_{39}-*b*-PEO_{36}–SA–trisNTA.d-Ni^{2+}	His_6-RFP	2.0 ± 0.4	16
PB_{39}-*b*-PEO_{36}–SA/PB_{39}-*b*-PEO_{36}–SA–trisNTA.d-Ni^{2+}	His_{10}-MBP-FITC	7.0 ± 1.2	15
PB_{39}-*b*-PEO_{36}–SA/PB_{39}-*b*-PEO_{36}–SA–trisNTA.d-Ni^{2+}	His_6-EGFP	12.3 ± 1.2	15
Ni^{2+}-NTA-NBD-lipid	His_6-peptide	4.3 ± 0.8	53
PB_{39}-*b*-PEO_{36}–SA/PB_{39}-*b*-PEO_{36}–SA–trisNTA.d-Cu^{2+}	His_6-tag	0.6 ± 0.2	this work

surface can be filled completely with peptides, explaining the small K_D value (Figure 1A,B). Additionally, the number of bound His_6-tags/vesicles agrees with the estimated number of available metal ions/vesicle surfaces calculated using the aggregation number from light scattering data.

Structure of the Coordination Sphere of Cu^{II} in His_6-tag-Cu^{II}-trisNTA Vesicles in Comparison to Model Systems. The X-band CW-EPR spectrum of functionalized polymeric vesicles is shown in Figure 5a. The observed broad signal has a very low intensity and is assumed to stem from a high local copper concentration due to the use of trisNTA and the large amount of Cu^{II}-binding functional groups on the surface of the vesicles. The strong dipolar interactions between the different Cu^{II} centers may broaden the EPR spectrum beyond detection. As a comparison, clear EPR spectra have already been reported for Cu^{II}-bound PB_{39}–PEO_{36}–SA-trisNTA.d.[15] The CW-EPR spectrum of the functionalized polymeric vesicles (Figure 5a) clearly differs from the spectrum simulated using the reported EPR parameters of the latter building blocks (Figure 5b). The spectrum in Figure 5a cannot be simulated assuming a single species, but exhibits spectral features characteristic of strong dipolar interactions between the Cu^{II} sites.

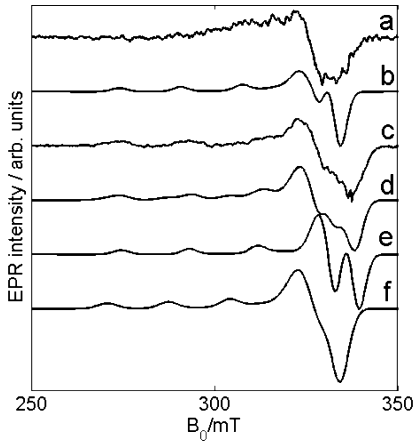

Figure 5. (a) X-band CW-EPR spectrum of a frozen solution of Cu^{II}-trisNTA functionalized vesicles in bidistilled water taken at 100 K. (b) Simulation of the CW-EPR spectrum of the PB_{39}–PEO_{36}–SA-trisNTA.d using the parameters reported in ref 15. (c) Experimental X-band CW-EPR spectrum of a frozen solution of Cu^{II}-trisNTA functionalized vesicles incubated with the His_6-strand peptide in a 1:50 ratio taken at 10 K. (d) Simulation of (c) using the parameters in Table 1. (e,f) Individual contributions to the simulation (d). All presented spectra are normalized for presentation means. The spectral intensity of (a) is more than a factor 10 smaller than that of (c).

In a next step, we added His_6-RFP, His_6-EGFP, and His_6-tags to the vesicles. Only the His_6-tags led to clear changes in the EPR spectra. The concentration of the His_6-proteins, limited by commercial availability, was found to be too low for EPR means. When EPR-suitable concentrated His_6-tags (2.0 mM) were added to the vesicle solution, the CW-EPR signal intensity increased, suggesting that the peptide functions as a spacer between the different Cu^{II} sites. The X-band CW-EPR spectrum of the vesicles incubated with the His_6-peptide is shown in Figure 5c together with its simulation (Figure 5d). Although this signal is still poorly resolved, two contributions can be discerned (EPR parameters are given in Table 2). The EPR parameters are typical of type II copper centers.[56] The first set of EPR parameters of the vesicle:His_6 system agrees with the case where Cu^{II} is equatorially ligated either to four oxygens (4O) or to one nitrogen and three oxygens (1N3O). The second set of parameters indicates that Cu^{II} is bound to either two nitrogens and two oxygens (2N2O), three nitrogens and one oxygen (3N1O), or four nitrogens (4N). The latter is in strong agreement with histidine binding to Cu^{II}, for which high values for the *z*-component of copper hyperfine have been reported.[57−61] Note that a third contribution stemming from the copper sites inside the vesicles will also still be present, but this contribution will be of considerably lower intensity in agreement with the spectrum in Figure 5a.

In order to correctly interpret the above findings, a number of model systems have been studied: (1) a mixture of Cu-triflate ($Cu(OTf)_2$) with NTA, (2) a mixture of $Cu(OTf)_2$ with His_6-peptide, and (3) a mixture of $Cu(OTf)_2$ with His_6-tags and NTA. The experiments are discussed in detail in the Supporting Information, and the corresponding EPR parameters are given in Table 2. Here, we summarize the main conclusions. The analysis revealed that the His_6-strand cannot bind to free Cu^{II} ions under the given conditions and that the spectral changes observed after addition of the His_6-tags to the vesicles (Figure 5) are not due to His_6 complexation of possible free Cu^{II} ions. Furthermore, the EPR experiments on different mixtures of $Cu(OTf)_2$, NTA, and His_6-peptide showed that both NTA and the His_6-peptide ligate to the Cu(II) ion. Furthermore, as the His_6-tag concentration increases, different Cu^{II} sites become linked by the His_6-tags.

For aqueous transition-metal complexes of NTA, a hexacoordination of the metal site is usually assumed (Figure 1C), involving ligation of three of the carboxy groups, the amine group and two water molecules. A similar binding mode is also proposed for the interaction between a polyhistidine tag and metal–NTA chelates, although no direct structural data are available. In fact, the crystal structure of a bis(imidazole) complexed to Cu^{II} and NTA revealed a five-coordinate square pyramidal structure, with protonation of one of the carboxy groups, equatorial ligation to two imidazoles and two carboxy groups of NTA, and weak axial coordination of the NTA amine group.[16]

In order to verify this, pulsed EPR experiments were undertaken. The low-frequency area of the HYSCORE spectrum of a $Cu(OTf)_2$:NTA (1:5) mixture shows no cross peaks from a weakly coupled ^{14}N nucleus,, which would be expected if the amine nitrogen is binding axially to the copper (see Supporting Information). The Mims ENDOR spectra

Table 2. Principal *g* and Copper Hyperfine Values of Cu^{II}-trisNTA Functionalized Vesicles in Comparison with Different Model Systems[a]

	g_x, g_y	g_z	$\|A_x\|,\|A_y\|$/MHz	$\|A_z\|$/MHz
Cu^{II} vesicles with His_6	2.035 (±0.004)	2.230 (±0.001)	5 (±20)	570 (±1)
	2.066 (±0.005)	2.215 (±0.001)	5 (±20)	590 (±2)
$Cu(OTf)_2$:NTA (1:5)	2.061 (±0.005)	2.302 (±0.001)	45 (±20)	512 (±2)
$Cu(OTF)_2$:His_6 (1:5)	2.074 (±0.005)	2.375 (±0.001)	21 (±20)	450 (±2)
$Cu(OTf)_2$:NTA:His_6 (1:5:5)	2.058 (±0.005)	2.282 (±0.001)	10 (±20)	510 (±2)
$PB_{39}PEO_{36}$–SA–trisNTA.d[2]	2.052	2.253	91	517
Cu(His) solution at pH 7.3[60]	2.058	2.24	37	561
Cu(His) solution at pH 3.8[57]	2.06	2.31	–	507

[a]The hyperfine values are given for the ^{63}Cu nucleus.

(Figure 6) and the ^1H HYSCORE spectra (Supporting Information) taken at different magnetic field positions show

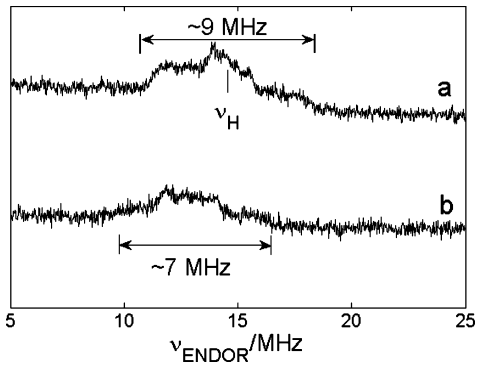

Figure 6. Mims-ENDOR of $Cu(OTf)_2$:NTA mixture of 1:5 ratio in frozen water solution recorded (a) at B_0 = 344.8 mT (observer position corresponding to $g \approx g_{x,y}$), and (b) at B_0 = 303.0 mT (observer position corresponding to $g = g_z$, $M_I = -1/2$).

maximum ^1H hyperfine couplings of 7–9 MHz. This agrees with the findings for $[Cu(H_2O)_6]^{2+}$ in frozen water[35] and in $Mg(NH_4)_2(SO_2)_4{\cdot}6H_2O$ crystals.[62] These data thus corroborate equatorial water ligation in the Cu^{II}–NTA complex. The large proton coupling is unlikely to stem from the NTA protons, because these protons are further away from the copper site and will result in smaller hyperfine couplings.

Davies ENDOR spectroscopy allowed probing of the interactions with the directly coordinated nitrogens (Supporting Information), revealing a value of ~25 MHz for the *z* component of the hyperfine interaction of the amine nitrogen, confirming equatorial ligation of this amine.

Upon the addition of His_6-tags to the $Cu(OTf)_2$:NTA mixture, the low-frequency HYSCORE spectra show contributions of a weakly coupled ^{14}N nucleus (Figure 7A) that can be simulated using the data in Table 3 (Figure 7B). The parameters are close to those reported for the remote imidazole nitrogen in Cu^{II}-bound imidazole complexes[63] and Cu^{II}-bound histidine complexes.[57,59,64,65] This confirms our earlier hypothesis from the CW-EPR results that the His_6-peptides are indeed binding. Furthermore, the maximum observed proton coupling in the Mims ENDOR and HYSCORE spectra is now reduced to approximately 5.8 MHz (see Supporting Information), agreeing with the known proton hyperfine coupling value for the H_ε proton of a histidine imidazole that is equatorially ligated to a copper ion (max. coupling 5.4 MHz[60]). This confirms that the His residue substitutes the equatorial water.

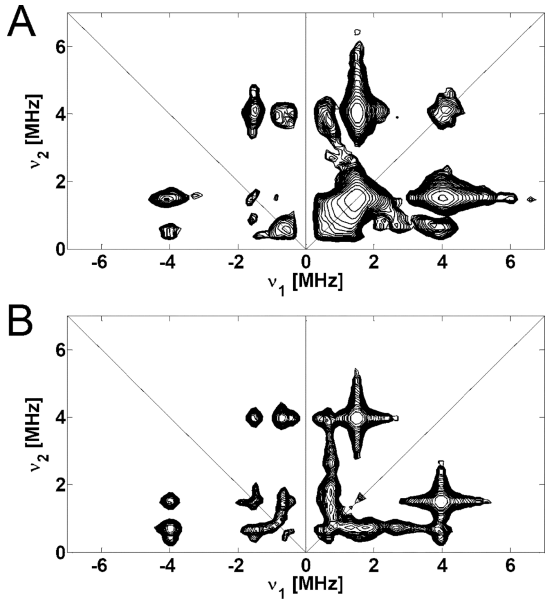

Figure 7. (A) X-band HYSCORE spectrum of a frozen solution of $Cu(OTf)_2$:NTA:His_6-peptide mixture at a 1:5:50 ratio taken at 5 K. (B) Simulation of (A) using the parameters from Table 3. The observer position is 335.0 mT, τ = 104 ns.

Table 3. Comparison between the Experimental ^{14}N Spin Hamiltonian Parameters Derived from the HYSCORE Spectra for His_6-tag Ligation and the Cu^{II}–NTA-Functionalized Vesicles and the Cu^{II}–NTA Complexes

	A/MHz	e^2qQ/h/MHz	η
Cu^{II} vesicles with His_6	±1.9 (±0.3)	±1.5 (±0.1)	0.95 (±0.10)
$Cu(OTf)_2$:NTA:His_6 (1:5:50)	±1.7 (±0.3)	±1.5 (±0.1)	0.90 (±0.10)
Cu(His)[18]	1.4	−1.43	0.95

The above pulsed EPR analysis of the model complexes can now be used to evaluate the effect of addition of His_6-tags to the Cu^{II}–NTA-functionalized vesicles. The spin echo of a frozen water solution of the vesicles without peptide was extremely weak and no pulsed EPR experiments could be performed. This agrees with the poor CW-EPR spectrum (Figure 5a). In agreement with the CW-EPR results, the echo intensity improves after the addition of the His_6-peptide, which may indicate that the peptide acts as a spacer between the Cu^{II} sites on the vesicle surface, reducing the dipolar interaction between these sites. Nevertheless, the echo intensity was still low and ESEEM or ENDOR experiments could only be performed at the position of highest echo intensity

dx.doi.org/10.1021/jp305544v | J. Phys. Chem. B 2012, 116, 10113–10124

(corresponding to the observer position $g = g_{x,y}$). Figure 8A shows the ^{14}N HYSCORE recorded at this observer position

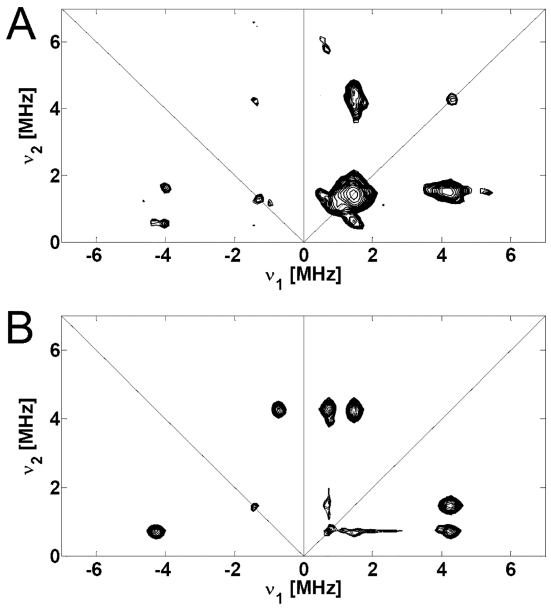

Figure 8. (A) X-band HYSCORE spectrum of a frozen solution of Cu^{II}–NTA-functionalized vesicles with His_6-peptide at a 1:50 ratio taken at 5 K. (B) Simulation of (A) using the parameters from Table 3. The observer position is 338.8 mT, τ = 120 ns.

with its corresponding simulation using the data given in Table 3 (Figure 8B). The parameters agree with the data expected for the remote nitrogen of a His ligand, confirming binding of the His_6-peptide to the copper site. The Mims- ENDOR experiments corroborate these conclusions (Supporting Information) and argue against equatorial H_2O ligation.

In summary, the above EPR analysis shows that both the aqueous Cu^{II}–NTA and the Cu^{II}–NTA–His_6 complexes are type II copper complexes. The pulsed EPR and ENDOR data show that the copper ion is equatorially bound to at least one water molecule and to the NTA amine nitrogen. This situation differs from that observed for the X-ray structure of copper(II) nitrilotriacetic acid–bis(*N*-methylimidazol-2-yl)ketone ternary complex, where the NTA amine binds in the axial position.[31] In the latter case, the use of a flat bis(imidazole) complex may be the cause of this different configuration. The HYSCORE and ENDOR data clearly show that the equatorial water is replaced by His residue(s) upon addition of His_6-strand peptides. Furthermore, the pulsed EPR data also confirm equatorial ligation of the imidazole(s) of the His_6-tags when the Cu^{II}–NTA moieties are attached to the surface of polymeric vesicles.

It is interesting to note that the CW-EPR results reveal the presence of two different type II copper sites after the addition of His_6-tags to the vesicles (Table 2). Furthermore, the two observed complexes have principal *g* and copper hyperfine values that significantly differ from those observed for the $Cu(OTf)_2$:NTA:His_6–peptide mixture. This may indicate that the vesicle does influence the local copper complex structure. In fact, the g_z value of Cu^{II}–PB_{39}–PEO_{36}–SA–trisNTA.d is also lower than that observed for the aqueous copper NTA complex. Interestingly, the EPR parameters of the vesicle/His_6-tag mixture resemble more those found for copper–histidine complexes at neutral pH,[60] while those of the $Cu(OTf)_2$:NTA:His_6–peptide mixture are more like those of the copper–histidine complexes at pH 3.82.[11] The difference between the copper–histidine ligation at different pH lies in the number of His residues (and amino groups) that ligate to the copper.

In order to complement the above observations, the EPR parameters of three models were computed using DFT. Although it is known that the state-of-the-art DFT does not yet reproduce EPR parameters of transition-metal complexes fully accurately (the *g* values tend to be underestimated and the transition-metal hyperfine values are usually not well reproduced), the computations tend to predict quite well the general trends and the hyperfine values of the ligand nuclei.[66] The models were chosen so as to probe the effect of the exchange of water by His residues and the impact of the overall charge of the complex on the EPR parameters. Model A involves ligation of one NTA and two water molecules to the copper site, while models B and C involve ligation of one NTA and a bis(imidazole) molecule with a peptide-like linker. In model C, all carboxy groups are deprotonated; in models A and B, one of the carboxy groups is protonated. In all cases, several starting geometries were tested for geometry optimization and the structure with the overall lowest energy was used. The models are shown in Figure 9, and the corresponding coordinates are given in the Supporting Information.

Table 4 shows the main DFT results. The corresponding spin density distributions are shown in the Supporting Information. Comparing the computed parameters of models A and B, we notice that a number of the experimentally observed trends are nicely reproduced by the DFT computations. Both complexes are characterized by a quasi-axial *g* tensor, typical for type II complexes with the copper in a $(d_{x^2-y^2})^1$ ground state. For the aqueous Cu^{II}–NTA model (model A), the computations confirm the experimental observation that the NTA amine nitrogen lies in the equatorial

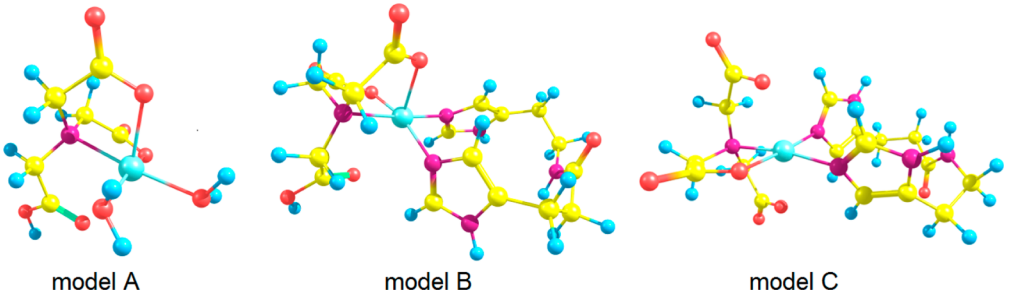

Figure 9. DFT-optimized structures of the three models. Model A: $[Cu(N(CH_2COO)_2(CH_2COOH))(H_2O)_2]$. Model B: $[Cu(N(CH_2COO)_2(CH_2COOH))(C_{11}H_{15}N_5O)]$. Model C: $[Cu(N(CH_2COO)_3)(C_{11}H_{15}N_5O)]^-$.

dx.doi.org/10.1021/jp305544v | *J. Phys. Chem. B* 2012, 116, 10113–10124

Table 4. Computed Principal *g* and Hyperfine Values for Models A–C (Figure 9)

	g_x	g_y	g_z	
model A	2.067	2.075	2.210	
model B	2.059	2.061	2.193	
model C	2.038	2.099	2.202	
	nucleus	A_x (MHz)	A_y (MHz)	A_z (MHz)
model A	Cu	69	77	−522
	N(NTA)	27	45	27
	H (H_2O)[a]	−10.8	6.2	−5.4
model B	Cu	49	76	−533
	N(NTA)	27	41	27
	N1(His)[b]	44	36	35
	N2(His)[c]	1.7	2.3	1.6
	H(His)[a]	6.4	−0.4	0.1
model C	Cu	173	−3	−495
	N(NTA)	20	33	20
	N1(His)[b]	42	34	33
	N2(His)[c]	1.6	2.2	1.6
	H (His)[a]	5.9	−0.3	0.2

[a]Data for the proton with the largest hyperfine coupling (in absolute value). [b]Average of computed hyperfine values of copper bound His nitrogens. [c]Average of computed hyperfine values for remote His nitrogens.

plane (i.e., plane determined by $d_{x^2-y^2}$) and bears a considerable amount of spin density. In fact, the computed *z* component of this hyperfine interaction (27 MHz) is very close to the experimental value (25 MHz). The maximum hyperfine interaction (absolute value) computed for the protons of the equatorially ligated water molecules (10.7 MHz) is of the order of the maximum proton hyperfine coupling observed experimentally (9 MHz). The computed maximum proton hyperfine couplings of the His residue (model B) are considerably smaller (6.4 MHz), mimicking the experimental trend. The hyperfine values of the remote nitrogens are indeed found to be on the order of 1.5–2.2 MHz. Furthermore, g_z is found to decrease upon attachment of the His residues and the copper $|A_z|$ values are very similar for both models A and B, in agreement with the experiment. In short, the relatively good agreement between the computed and the experimental trends confirms that the change in EPR parameters upon addition of His_6 tags to $Cu(OTf)_2$:NTA is entirely due to the replacement of the equatorial water by His residues.

In a next step, we evaluated the effect of the protonation of the NTA carboxy groups by comparing model B (one protonated carboxy group) and model C (no protonation of the carboxy groups). Deprotonation of the third carboxy group induces an increase in the g_z value and the *g* tensor becomes more rhombic. Furthermore, the copper $|A_z|$ value and the NTA amine nitrogen hyperfine coupling are considerably lowered, while the rest of the ligand hyperfine values are affected to a smaller degree (on the order of that of the experimental errors). This suggests that protonation may be one of the cause(s) of the difference between the EPR parameters of $Cu(OTf)_2$–NTA–His_6 mixture and the vesicle–His_6 systems. Indeed, for both cases, very similar hyperfine values were found for the protons and remote nitrogens of the His residue, as is also computed for models B and C. The g_z values ($|A_z|$ values) of the vesicle case are lower (higher) than for the $Cu(OTf)_2$–NTA–His_6 mixture. Moreover, the difference in the copper A_z values is higher between these two His_6-ligated cases than between $Cu(OTf)_2$–NTA and $Cu(OTf)_2$–NTA–His_6. Similarly, the difference in the copper A_z value is larger between models B and C than between models A and B. This all points to an increased protonation of the NTA carboxy groups in the vesicle case, possibly induced by vesicle surface properties. The observation of two different copper complexes in the vesicle case may be due to changes in the number or orientation of the His ligands.

CONCLUSION

We have shown that Cu^{II}–trisNTA-functionalized vesicles are well suited to serve as supramolecular assemblies for efficient peptide binding. An oligohistidine sequence consisting of six histidines, a His_6-tag, has been used as a simple model for His-tag proteins to allow the investigation of binding to copper centers exposed at the surface of nanovesicles. A detailed structural view of the rearrangement of the metal coordination sphere upon binding of His_6-tags via molecular recognition was obtained. More than 200 fluorescently labeled His_6-tags were bound to one vesicle, which is more than previously reported for His-tag proteins. This explains the highly intense fluorescence corona appearing around vesicles in fluorescence microscopy. From FCS measurements, a high binding affinity is demonstrated, which is an order of magnitude higher than previously reported for His-tag proteins.[15,16] The electronic and geometric change in the copper center was studied by different EPR and ENDOR methods under conditions in which the His_6-tag was bound to the Cu^{II} center in the NTA pocket. Using the EPR and DFT data from the model systems, His_6-tag binding was recognized via the typical HYSCORE signature of the remote nitrogen of the imidazole ligand of the residue, and by the reduction of the proton hyperfine coupling. These features confirmed the strong, specific binding of these peptides to the metal centers exposed at the surface of functionalized vesicles. The difference between the principal *g* and copper hyperfine values of the His_6-bound functionalized vesicles and those of simple Cu^{II}–NTA–His_6 models may be due to the difference in protonation of the NTA carboxy groups, as indicated by DFT. The highly selective binding capacity of the copper-functionalized PB-*b*-PEO vesicles together with a simple preparation procedure and outstanding stability makes the system very promising for applications such as protein crystallization, targeting approaches, or immobilization on solid support. In order to address these medical applications we will further develop and test our system in physiological relevant conditions, as for example in simulated biological fluids.

ASSOCIATED CONTENT

Supporting Information

(1) Light scattering data, (2) FCS data calculations, (3) detailed CW-EPR, HYSCORE and ENDOR analyses of the different systems under study, and (4) the coordinates of DFT-optimized geometries of different model structures. This material is available free of charge via the Internet at http://pubs.acs.org.

AUTHOR INFORMATION

Corresponding Author

*E-mail: cornelia.palivan@unibas.ch.

Author Contributions

The manuscript was written through contributions of all authors. All authors have given approval to the final version of the manuscript.

Notes

The authors declare no competing financial interest.

■ ACKNOWLEDGMENTS

This work was supported by the Swiss National Science Foundation (grant 205321_124406), and by NCCR Nanosciences and this is gratefully acknowledged. P.T. thanks COST P15 Action for providing financial support for a Short Term Scientific Mission at the University of Antwerp. S.V.D. acknowledges the Hercules Foundation (grant AUHA013). M.E. thanks the University of Antwerp (BOF-UA) for Ph.D. funding, and P.T. thanks Dr. Dirk De Bruyn for help in synthesizing and analyzing the His_6-tags. The authors thank Mark Inglin for reading the manuscript.

■ REFERENCES

(1) Egli, S.; Schlaad, H.; Bruns, N.; Meier, W. *Polymers* **2011**, *3*, 252−280.
(2) Baumann, P.; Tanner, P.; Onaca, O.; Palivan, C. G. *Polymers* **2011**, *3*, 173−192.
(3) Tanner, P.; Baumann, P.; Enea, R.; Onaca, O.; Palivan, C.; Meier, W. *Acc. Chem. Res.* **2011**, *44*, 1039−1049.
(4) Antonietti, M.; Foerster, S. *Adv. Mater.* **2003**, *15*, 1323−1333.
(5) Discher, D. E.; Eisenberg, A. *Science* **2002**, *297*, 967−973.
(6) Egli, S.; Nussbaumer, M. G.; Balasubramanian, V.; Chami, M.; Bruns, N.; Palivan, C.; Meier, W. *J. Am. Chem. Soc.* **2011**, *133*, 4476−4483.
(7) Buckland, R. M. *Nature (London)* **1986**, *320*, 557−558.
(8) Conroy, P. J.; Hearty, S.; Leonard, P.; O'Kennedy, R. J. *Seminars Cell Dev. Biol.* **2009**, *20*, 10−26.
(9) Sine, S. M. *J. Neurobiol.* **2002**, *53*, 431−446.
(10) Jamieson, A. C.; Wang, H.; Kim, S.-H. *Proc. Natl. Acad. Sci. U.S.A.* **1996**, *93*, 12834−12839.
(11) Hochuli, E.; Döbeli, H.; Schacher, A. *J. Chromatogr. A* **1987**, *411*, 177−184.
(12) Terpe, K. *Appl. Microbiol. Biotechnol.* **2003**, *60*, 523−533.
(13) Dietrich, C.; Schmitt, L.; Tampe, R. *Proc. Natl. Acad. Sci. U.S.A.* **1995**, *92*, 9014−9018.
(14) Gamsjaeger, R.; Wimmer, B.; Kahr, H.; Tinazli, A.; Picuric, S.; Lata, S.; Tampe, R.; Maulet, Y.; Gruber, H. J.; Hinterdorfer.; et al. *Langmuir* **2004**, *20*, 5885−5890.
(15) Nehring, R.; Palivan, C. G.; Casse, O.; Tanner, P.; Tuxen, J.; Meier, W. *Langmuir* **2008**, *25*, 1122−1130.
(16) Nehring, R.; Palivan, C. G.; Moreno-Flores, S.; Mantion, A.; Tanner, P.; Toca-Herrera, J. L.; Thuenemann, A.; Meier, W. *Soft Matter* **2010**, *6*, 2815−2824.
(17) Hoffmann, C.; Gaietta, G.; Zurn, A.; Adams, S. R.; Terrillon, S.; Ellisman, M. H.; Tsien, R. Y.; Lohse, M. J. *Nat. Protocols* **2010**, *5*, 1666−1677.
(18) Soh, N. *Sensors* **2008**, *8*, 1004−1024.
(19) Wilchek, M.; Bayer, E. A. *Immobilized Biomol. Anal.* **1998**, 15−34.
(20) He, H.; Uray, G.; Wolfbeis, O. S. *Anal. Lett.* **1992**, *25*, 405−414.
(21) Perinoto, A. C.; Maki, R. M.; Colhone, M. C.; Santos, F. R.; Migliaccio, V.; Daghastanli, K. R.; Stabeli, R. G.; Ciancaglini, P.; Paulovich, F. V.; de Oliveira, M. C. F.; Oliveira, O. N., Jr.; Zucolotto, V. *Anal. Chem.* **2010**, *82*, 9763−9768.
(22) Knecht, S.; Ricklin, D.; Eberle, A. N.; Ernst, B. *J. Mol. Recogn.* **2009**, *22*, 270−279.
(23) Stadlbauer, S.; Riechers, A.; Späth, A.; König, B. *Chem.−Eur. J.* **2008**, *14*, 2536−2541.
(24) Vomasta, D.; Högner, C.; Branda, N. R.; König, B. *Angew. Chem., Int. Ed.* **2008**, *47*, 7644−7647.
(25) André, T.; Reichel, A.; Wiesmüller, K.-H.; Tampé, R.; Piehler, J.; Brock, R. *ChemBioChem* **2009**, *10*, 1878−1887.
(26) Lata, S.; Piehler, J. *Anal. Chem.* **2005**, *77*, 1096−1105.
(27) Lata, S.; Reichel, A.; Brock, R.; Tampe, R.; Piehler, J. *J. Am. Chem. Soc.* **2005**, *127*, 10205−10215.
(28) Huang, Z.; Hwang, P.; Watson, D. S.; Cao, L.; Szoka, F. C. *Bioconjugate Chem.* **2009**, *20*, 1667−1672.
(29) Lata, S.; Gavutis, M.; Tampé, R.; Piehler, J. *J. Am. Chem. Soc.* **2006**, *128*, 2365−2372.
(30) Xxxx, Y.; Xxxx, Y.; Xxxx, Y.; Xxxx, Y. *J. Chin. Chem. Soc.* **2005**, *52*, 1281−1290.
(31) Burns, C. J.; Field, L. D.; Hambley, T. W.; Lin, T.; Ridley, D. D.; Turner, P.; Wilkinson, M., P. *ARKIVOC* **2001**, *vii*, 157−165.
(32) Murphy, B.; Hathaway, B. *Coord. Chem. Rev.* **2003**, *243*, 237−262.
(33) Stoll, S.; Schweiger, A. *J. Magn. Reson.* **2006**, *178*, 42−55.
(34) Davies, E. R. *Phys. Lett. A* **1974**, *47*, 1−2.
(35) Schosseler, P. M.; Wehrli, B.; Schweiger, A. *Inorg. Chem.* **1997**, *36*, 4490−4499.
(36) Hoefer, P.; Grupp, A.; Nebenfuehr, H.; Mehring, M. *Chem. Phys. Lett.* **1986**, *132*, 279−282.
(37) Madi, Z. L.; Van, D. S.; Schweiger, A. *J. Magn. Reson.* **2002**, *154*, 181−191.
(38) Neese, F. *J. Chem. Phys.* **2001**, *115*, 11080−11096.
(39) Neese, F. *J. Phys. Chem. A* **2001**, *105*, 4290−4299.
(40) Neese, F. *J. Chem. Phys.* **2003**, *118*, 3939−3948.
(41) Neese, F. *J. Chem. Phys.* **2005**, *122*, 34107−34120.
(42) Becke, A. D. *Phys. Rev. A* **1988**, *38*, 3098−3100.
(43) Perdew, J. P. *Phys. Rev. B* **1986**, *33*, 8822−8824.
(44) Perdew, J. P. *Phys. Rev. B* **1986**, *34*, 7406−7406.
(45) Schäfer, A.; Horn, H.; Ahlrichs, R. *J. Chem. Phys.* **1992**, *97*, 2571−2577.
(46) Ahlrichs, R. The Ahlrichs (2df, 2pd) polarization functions are obtained from the TurboMole basis set library under ftp.chemie.uni-karlsruhe.de/pub/basen.
(47) Stephens, P. J.; Devlin, F. J.; Chabalowski, C. F.; Frisch, M. J. *J. Phys. Chem.* **1994**, *98*, 11623−11627.
(48) Barone, V. In *Recent Advances in Density Functional Methods*; Chong, D. P., Ed.; World Scientific Publ. Co.: Singapore, 1996; pp 287−334.
(49) Wachters, A. *J. Chem. Phys.* **1970**, *52*, 1033−1036.
(50) Sinnecker, S.; Rajendran, A.; Klamt, A.; Diedenhofen, M.; Neese, F. *J. Phys. Chem. A* **2006**, *110*, 2235−2245.
(51) Stauch, O.; Schubert, R.; Savin, G.; Burchard, W. *Biomacromolecules* **2002**, *3*, 565−578.
(52) Gruenwald, D.; Cardoso, M. C.; Leonhardt, H.; Buschmann, V. *Curr. Pharm. Biotechnol.* **2005**, *6*, 381−386.
(53) Dorn, I. T.; Neumaier, K. R.; Tampe, R. *J. Am. Chem. Soc.* **1998**, *120*, 2753−2763.
(54) Schmitt, L.; Ludwig, M.; Gaub, H. E.; Tampé, R. *Biophys. J.* **2000**, *78*, 3275−3285.
(55) Kent, M. S.; Yim, H.; Sasaki, D. Y.; Satija, S.; Seo, Y.-S.; Majewski, J. *Langmuir* **2005**, *21*, 6815−6824.
(56) Peisach, J.; Blumberg, W. E. *Arch. Biochem. Biophys.* **1974**, *165*, 691−708.
(57) Baute, D.; Arieli, D.; Neese, F.; Zimmermann, H.; Weckhuysen, B. M.; Goldfarb, D. *J. Am. Chem. Soc.* **2004**, *126*, 11733−11745.
(58) Drew, S. C.; Noble, C. J.; Masters, C. L.; Hanson, G. R.; Barnham, K. J. *J. Am. Chem. Soc.* **2009**, *131*, 1195−1207.
(59) Grommen, R.; Manikandan, P.; Gao, Y.; Shane, T.; Shane, J. J.; Schoonheydt, R. A.; Weckhuysen, B. M.; Goldfarb, D. *J. Am. Chem. Soc.* **2000**, *122*, 11488−11496.
(60) Manikandan, P.; Epel, B.; Goldfarb, D. *Inorg. Chem.* **2001**, *40*, 781−787.
(61) Valko, M.; Morris, H.; Mazúr, M.; Telser, J.; McInnes, E. J. L.; Mabbs, F. E. *J. Phys. Chem. B* **1999**, *103*, 5591−5597.
(62) Atherton, N. M.; Horsewill, A. J. *Mol. Phys.* **1979**, *37*, 1349−1361.

(63) Hunt, M. J.; Mackay, A. L.; Edmonds, D. T. *Chem. Phys. Lett.* **1975**, *34*, 473−475.
(64) Van Doorslaer, S.; Cereghetti, G. M.; Glockshuber, R.; Schweiger, A. *J. Phys. Chem. B* **2001**, *105*, 1631−1639.
(65) van Gastel, M.; Coremans, J. W. A.; Jeuken, L. J. C.; Canters, G. W.; Groenen, E. J. J. *J. Phys. Chem. A* **1998**, *102*, 4462−4470.
(66) Neese, F. *Anglais* **2009**, *253*, 526−563.